




Article

Hydrogen diffusion mechanisms in quartz: insights from H–Li, ²H–H and ²H–H–Li exchange experiments

Michael C. Jollands^{1,2,3*} , Peter M. E. Tollan^{4,5}, Lukas P. Baumgartner¹ and Othmar Müntener¹

¹Institute of Earth Sciences, University of Lausanne, Géopolis, 1005 Lausanne, Switzerland; ²Lamont-Doherty Earth Observatory, 61 Rt. 9W, Palisades, NY 10964, USA;

³Gemological Institute of America, 50 W. 47th St, New York, NY 10036, USA†; ⁴Institute of Geological Sciences, University of Bern, Baltzerstrasse 3, 3012 Bern, Switzerland; and ⁵Department of Earth Sciences, ETH Zürich, Sonneggstrasse 5, 8092 Zürich, Switzerland

Abstract

The diffusivity and diffusion mechanisms of hydrogen together with deuterium and lithium, parallel to the *c* axis of quartz, were investigated experimentally at 800°C, 0.1 GPa with the activity of H₂O or ²H₂O ≈ 1 [²H is used throughout this work to describe deuterium rather than D, to avoid confusion with the diffusion coefficient, *D*]. The pH was set using mixtures of H₂O (or ²H₂O) and HCl. Three types of experiment were conducted: (1) H-in/Li-out; (2) ²H-in/H-out; and (3) ²H-in/H + Li out, using three different natural quartz crystals as starting materials. Profiles of H, ²H and Li were measured using Fourier-transform infrared (FTIR) spectroscopy and laser ablation inductively coupled plasma mass spectrometry (LA-ICP-MS). H, ²H and Li are charge-compensated by Al³⁺ replacing Si⁴⁺, or by excess O²⁻. The total atomic concentration of monovalent cations appears to remain constant over the duration of the experiments. The resulting diffusion profiles are different for the three experimental designs and three starting materials, and some show complex shapes inconsistent with simple diffusion. A multi-site diffusion–reaction model is developed, with the theory based on previous models that have been derived mainly on the basis of conductivity measurements. In these models, the monovalent cations move away from their charge-balancing ion then diffuse rapidly to another site. The mobility of the monovalent cations is described by both a diffusion coefficient and an equilibrium constant that enables dissociation of the immobile charge-balanced defects. This model can describe complex step-shaped profiles formed in H-in/Li-out experiments, profiles with local maxima ('humped' profiles) in ²H-in/H + Li out experiments, and error function-shaped profiles in ²H-in/H-out and previously published Li-in/H-out experiments. Our data provide support for models previously proposed for quartz. Studies of the lengths and forms of diffusion profiles from such experiments provide a useful complement to assertions from conductivity experiments.

Keywords: quartz, diffusion, Fourier transform infrared spectroscopy, point defects

(Received 24 September 2021; accepted 29 December 2021; Accepted Manuscript published online: 7 January 2022; Associate Editor: Juraj Majzlan)

Introduction

Understanding how monovalent cations substitute into quartz, as well as how rapidly, and how, they move, is important for considerations including electrical conductivity (Verhoogen, 1952; Hughes, 1975; Jain and Nowick, 1982), diffusion chronometry or more generally quartz compositional heterogeneity in volcanic systems (Biró *et al.*, 2016; Tollan *et al.*, 2019), the fidelity of quartz hosted melt and fluid inclusions (Rottier *et al.*, 2017; Myers *et al.*, 2019), quartz rheology (Griggs and Blacic, 1965; Mackwell and Paterson, 1985) and purification or controlled alteration of quartz by electro-diffusion 'sweeping' (King, 1959; Brown *et al.*, 1980).

For these reasons, much experimental work has concentrated on obtaining independent determinations of the diffusion

coefficients of the monovalent cations, mainly focussed on H and its isotopes (Kats, 1962; Shaffer *et al.*, 1974; Kronenberg *et al.*, 1986; Rovetta *et al.*, 1989; Bachheimer, 1998; Jollands *et al.*, 2020a) though also including Li, Na and K (Verhoogen, 1952; Rybach and Laves, 1967; Frischat, 1970; Shaffer *et al.*, 1974; Sartbaeva *et al.*, 2004; Rottier *et al.*, 2017), as well as their substitution mechanisms (Staats and Kopp, 1974; Sibley *et al.*, 1979; Halliburton *et al.*, 1981; Hosaka and Taki, 1981; Aines and Rossman, 1984; Paterson, 1986; Stalder and Konzett, 2012; Baron *et al.*, 2015; Frigo *et al.*, 2016; Müller and Koch-Müller, 2018; Potrafke *et al.*, 2019; Jollands *et al.*, 2020b). The fact that the system remains the target of active study >130 years after the first published conductivity measurements in quartz (Tegetmeier and Warburg, 1887; Curie, 1889), which were more-or-less contemporaneous with the first observations of the presence of O–H groups within quartz (Merritt, 1895; Königsberger, 1897), is testament to its importance. For more information regarding H incorporation and diffusion in quartz, as well as various physical, chemical and geological implications, see the recent review by Stalder (2021).

*Author for correspondence: Michael C. Jollands, Email: m.c.jollands@gmail.com

†Present address.

Cite this article: Jollands M.C., Tollan P.M.E., Baumgartner L.P. and Müntener O. (2022) Hydrogen diffusion mechanisms in quartz: insights from H–Li, ²H–H and ²H–H–Li exchange experiments. *Mineralogical Magazine* 86, 112–126. <https://doi.org/10.1180/mgm.2021.105>

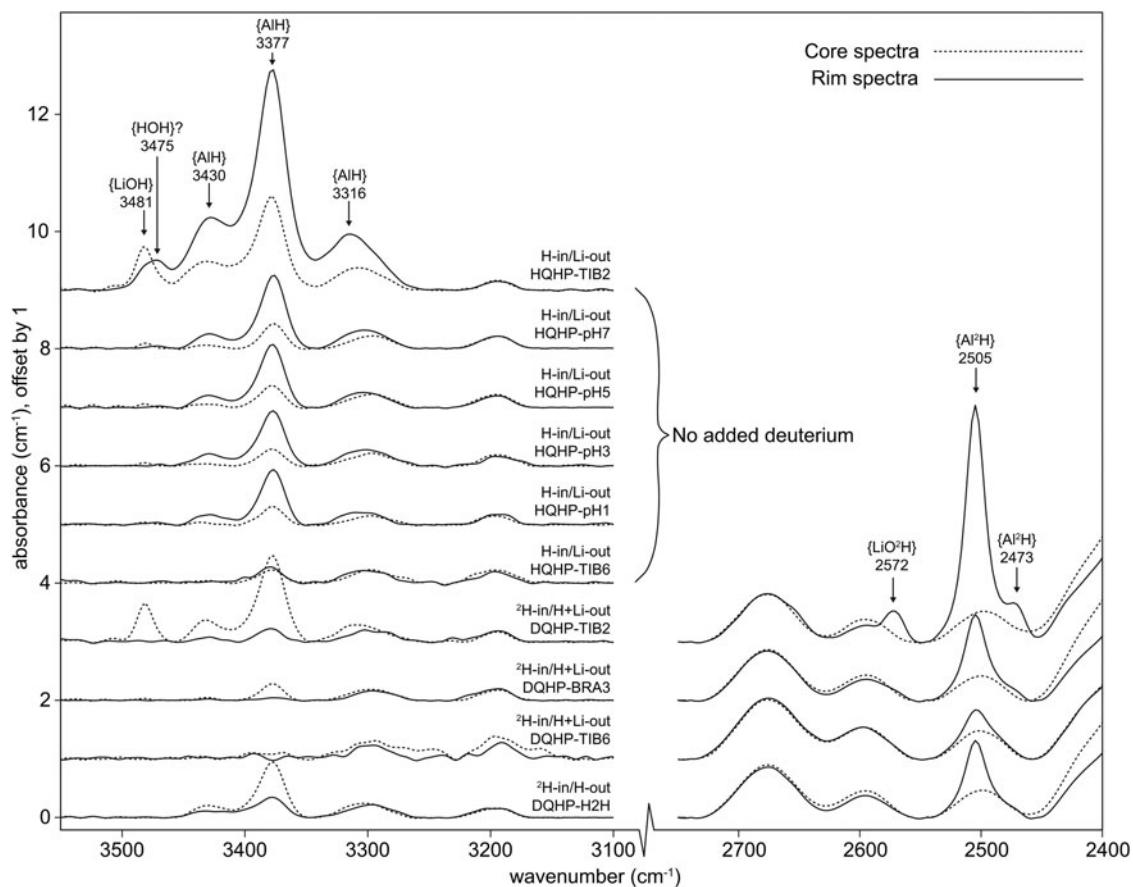


Fig. 1. Example spectra (total absorbance) from cores (dotted lines) and rims (solid lines) from all experiments. Both the O–H and O–²H stretching regions are shown, where appropriate.

Notwithstanding the considerable amount of research, absent from the literature are descriptions of experiments wherein H is diffused into quartz at elevated pressure and temperature, and the resulting profiles of H content versus distance are measured using Fourier-transform infrared (FTIR) spectroscopy. This technique has now become widely accepted as a tool for considering H diffusion in other nominally anhydrous minerals (e.g. Demouchy and Mackwell, 2006). Not only can diffusion coefficients be determined using this method, but the contributions of individual H-bearing defects to total H can be resolved, and the specific shapes of profiles in concentration vs. distance space can be used to elucidate diffusion mechanisms.

The diffusion of H in quartz has been proposed to occur by the movement of H along some fast pathway, followed by immobilisation of that H when it moves into association with stationary Al (Hughes, 1975; Jain and Nowick, 1982; Kronenberg and Kirby, 1987). This is discussed in more detail below, though, importantly, the corollary of invoking such a diffusion mechanism would be diffusion profile forms that do not necessarily correspond to error-function shapes (e.g. Dohmen *et al.*, 2010; Bloch *et al.*, 2020). However, in our previous study (Jollands *et al.* 2020a), where H was diffused out of quartz, coupled with in-diffusion of Li or Na, we consistently observed profiles that could be fitted to error-function forms. This discrepancy between prediction and observation forms the motivation for the present study, which describes experiments that can be considered broadly as the reverse of those presented by Jollands *et al.*

(2020a) i.e. wherein H, or ²H*, is diffused into quartz crystals rather than being diffused out.

Herein, experiments are described wherein different natural quartz crystals containing trace concentrations of H and Li were annealed at 800°C and 0.1 GPa together with H₂O or ²H₂O at controlled pH. These experiments show H or ²H gain into, and Li loss out of, the quartz crystals. Regardless of the relatively simple experimental design, the diffusion profiles of H (and ²H, Li) are complex, and rarely conform to error-function shapes. These results can be explained by invoking the aforementioned model (Hughes, 1975; Jain and Nowick, 1982; Kronenberg and Kirby, 1987), which are also capable of explaining qualitatively why simple error-function forms were observed by Jollands *et al.* (2020a).

Methods

Starting materials

Cubes cut from three of the crystals used and characterised in a previous study considering H diffusion in quartz (Jollands *et al.*, 2020a) were again used for this study. These were two sections of a single quartz slab cut from two Tibetan crystals (TIB2 and TIB6), and a crystal of Brazilian quartz (BRA3). In the

*²H is used throughout to describe deuterium rather than D, to avoid confusion with the diffusion coefficient, *D*.

Table 1. Experimental conditions. Each entry in the ‘Experiment’ column represents a single run. Some of the runs contained multiple crystals, these are each given individual sample IDs (final column). The experiment labelled ‘Pre-eq.’ was the pre-equilibration step before the H-²H exchange experiment (H²H). HCl was 1 M.

Series	Experiment	T (°C)	P (GPa)	t (hr)	Fluid composition	Nominal pH	pH (expt. P, T)	Crystals used	Sample ID
H-in/Li-out	‘pH1’	800	0.1	1	HCl-milliQ	1	5.39	BRA3	HQHP-pH1
	‘pH3’	800	0.1	1	HCl-milliQ	3	6.38	BRA3	HQHP-pH3
								TIB2	HQHP-TIB2
								TIB6	HQHP-TIB6
								BRA3	HQHP-pH5
	‘pH7’	800	0.1	1	milliQ	7	6.9	BRA3	HQHP-pH7
	²H-in / H + Li out	‘DQHP’	800	0.1	1	HCl- ² H ₂ O	3	6.38	BRA3
TIB2									DQHP-TIB2
TIB6									DQHP-TIB6
²H-in / H-out	‘Pre-eq.’	800	0.1	53.5	HCl-milliQ	3	6.38	BRA3	N/A
	‘H ² H’	800	0.1	1	HCl- ² H ₂ O	3	6.38	BRA3	DQHP-H ² H

previous study, TIB2 is denoted Q2, and TIB6 is Q6, both cut from crystal ‘TIB’. BRA3 was denoted Q5. These were chosen to represent a variety of H and Li contents. TIB2 has the highest H + Li, TIB6 the lowest and BRA3 is intermediate.

The only notable trace elements in these materials, as measured in Jollands *et al.* (2020a), are Al, Li, B, Ti and H. Generally Na and K were below detection limits. It is not possible to give initial concentrations in the exact crystals used for experiments, though concentration ranges for detected trace elements in the starting materials overall (wt. ppm) were: TIB2: 55–83 Al, 7.4–9.5 Li, 0.19–0.39 B, 0.23–0.53 Ti; TIB6: 2.1–13 Al, 0.4–1.6 Li; and BRA3: 9.4–21 Al, 2.1–3.6 Li, 0.08–0.5 Ti. Using the Thomas *et al.* (2009) absorption coefficient for quartz, the mean H contents for the starting materials (mean spectrum, extracted from the FTIR maps in figure 1a of Jollands *et al.* (2020a), then resolved to remove non-OH components), as wt. ppm H₂O, are: TIB2 12.0; TIB6 1.5; BRA3 3.6. As the cubes were cut from areas of larger crystals chosen due for their homogeneity in terms of H₂O content, there is no reason to assume any systematic gradients in any trace-element contents (e.g. pre-existing diffusion profiles, or other concentration profiles).

Experimental methods

Hydrogen in-, lithium-out (H-in/Li-out) experiments

These and all other experiments were conducted at the University of Lausanne. Gold tubing of 4.5 mm O.D. and 4.1 mm I.D. was cut into 20–35 mm lengths, which were cleaned using acetone, then triple crimped and welded at one end. The open capsules were then annealed over a propane flame, then cleaned with boiling concentrated HCl, acetone then ethanol and dried at 60°C. They were then packed with SiO₂ powder, together with ~1.5 mm cubes of quartz and ~20 µL of milliQ or HCl-milliQ mixes to give room temperature and pressure pH of 1, 3, 5 or 7. One experiment was run at each pH condition. The experiments at pH1, pH5 and pH7 contained only one crystal of BRA3 – these samples are denoted HQHP-pH1, HQHP-pH5 and HQHP-pH7, respectively. The experiment at pH3 contained one crystal each of BRA3, TIB2 and TIB6, with the samples denoted HQHP-pH3, HQHP-TIB2 and HQHP-TIB6, respectively. Further experimental details are provided in Table 1. At run conditions, the pH values are 5.39, 6.38, 6.88 and 6.90, respectively (see column ‘pH (expt. P, T)’ in Table 1), with log₁₀K for the dissociation reactions of H₂O (–13.8) and HCl (–9.79) calculated using SUPCRT (Johnson

et al., 1992). Values obtained were extrapolated using the density correlation approach (Eugster and Baumgartner, 1987; Manning 1994; Dolejs and Manning, 2010). The program *Soluble* (Roselle and Baumgartner, 1995) was used to calculate pH, using a Debye-Hückel activity model. Values of the pH in the text herein, refer to pH at room temperature (i.e. 1, 3, 5 and 7).

The open ends of the capsules were then flat crimped, welded closed, weighed, and left for >12 hr at ~110°C, then reweighed to verify no mass loss. Charges were loaded into cold-seal pressure vessels which were pressurised (0.1 GPa, N₂ pressure medium), and pre-heated to 800°C, with temperatures monitored using type-K thermocouples (further information is provided in the Supplementary Appendix, see below for details). The capsule was then introduced into the hot spot and left for 1 hr using a magnetic system (e.g. Matthews *et al.*, 2003). At the end of the runs, the samples were removed from the hot spot and the bombs were cooled down by blowing with compressed air – thus cooling from run temperature to <200°C in a few minutes. The vessels were then depressurised and charges were recovered and re-weighed to ensure that water was retained through the experiment. Capsules were then opened and the crystals, none of which were cracked, were recovered and mounted in 1 inch epoxy discs, with the *c* axis of the crystal in the plane parallel to the face of the disc.

The epoxy discs were then prepared as thick sections (~400 µm thickness) for FTIR spectroscopy, ensuring that the section represented approximately the core of the quartz cube. One side was polished (1–3 µm diamond) and the other side was flattened with alumina slurry (>15 µm grit) only. It was found that the latter preparation gave more consistent ablation behaviour when conducting laser ablation inductively coupled plasma mass spectrometry (LA-ICP-MS) analyses with our system.

Deuterium-in, hydrogen-out (²H-in/H-out) experiment

This experiment is denoted HQHP-H²H. For a true H-²H exchange experiment, the only exchange should be between H and ²H. Thus, Li or other monovalent cations should be eliminated from the crystal before the experiment. Such experiments must be undertaken in two steps, firstly to equilibrate (or metastably equilibrate) fully the crystal with H at the run conditions, followed by exchange with ²H (e.g. Kurka *et al.*, 2005; Novella *et al.*, 2017).

To this end, crystals of BRA3 were placed into Au capsules with a H₂O–HCl mix at pH3, welded, as above, then annealed

at 800°C, 0.1 GPa for 53.5 hr. The crystals were then recovered, as above. One crystal was doubly polished and analysed for homogeneity by FTIR spectroscopy (further information is provided in the Supplementary Appendix).

One other crystal was then placed into an Au capsule with nearly pure $^2\text{H}_2\text{O}$ and welded closed, as with the H-in/Li-out experiments. To set the pH, and to avoid large changes in the H/ ^2H ratio of the $^2\text{H}_2\text{O}$, 0.6 μL of 1 M HCl was added to a 0.6 mL vial of $^2\text{H}_2\text{O}$ (99.99%, Sigma Aldrich) as it was opened. Capsules were filled and welded within ~ 2 hr of opening the vial of $^2\text{H}_2\text{O}$, which was not re-used, so H- ^2H exchange with the atmosphere should be negligible. This experiment was then run as with the H-in/Li-out experiments, for 1 hr at 800°C, 0.1 GPa. Following the experiment, the crystal was mounted in epoxy and prepared for FTIR and LA-ICP-MS analyses, as above.

Deuterium-in, hydrogen and lithium-out (^2H -in/H + Li out) experiments

The experimental method was a hybrid of the H-in/Li-out and ^2H -in/H-out experiments. Crystals of TIB2, TIB6 and BRA3 were welded into an Au capsule with SiO_2 powder and pH3 $^2\text{H}_2\text{O}$, then run at 0.1 GPa, 800°C for 1 hr, and the crystals were recovered and prepared as above. The samples are denoted DQHP-TIB2, DQHP-TIB6 and DQHP-BRA3. For reasons described above, these experiments cannot be considered as H- ^2H exchange experiments given the presence of Li in the starting material.

Analytical methods

FTIR spectroscopy

FTIR spectra were recorded at the University of Bern using a Bruker Tensor II spectrometer coupled to a Bruker Hyperion 3000 microscope, equipped with an XYZ imaging stage and a dry air-purged analytical chamber. Spectra were recorded (32–128 scans, 8 cm^{-1} resolution) using a single mercury cadmium telluride (MCT) detector, with a $25\text{--}40\ \mu\text{m} \times 150\text{--}200\ \mu\text{m}$ on-sample aperture, with the long axis oriented parallel to the crystal edge. Such FTIR analyses sample a Gaussian volume within the sample (Ni and Zhang, 2008) with a full width at half maximum that may be considerably larger than the apparent sampling width determined by the nominal aperture size. Therefore, the diffusion coefficients reported herein can be considered maxima due to convolution effects (e.g. Jibamitra *et al.*, 1988; Jollands, 2020). Spectra were recorded every $\sim 10\text{--}20\ \mu\text{m}$ along a 1D profile parallel to the c axis. Whilst some profiles were also measured perpendicular to the c axis, the effective diffusion distances were generally only several tens of micrometres. This is to be expected, given the extreme anisotropy of diffusion for monovalent cations in quartz (e.g. Verhoogen, 1952; Frischat, 1970; Jollands *et al.*, 2020a), where diffusion parallel to the c axis is considerably faster than diffusion perpendicular to c . This effectively precludes quantitative descriptions of diffusivity or diffusion mechanisms perpendicular to the c axis – such short profiles will be strongly affected by convolution artefacts. Qualitatively though, this is in line with previous demonstrations of the diffusive anisotropy of H.

Data were processed by baseline subtraction using a concave rubberband algorithm (built into Bruker OPUS software) with 256 baseline points and 3 iterations. Further information is provided in the Supplementary Appendix. Correction to 1 cm thickness was done on baseline uncorrected data, using the

Table 2. The defects described in this study presented in shorthand notation together with their end-member formulae, as well as their description in Kröger-Vink notation. The latter is presented in two ways, one in which the H, ^2H or Li are denoted simply as ‘interstitial’ with an ‘i’, and the other where the H or ^2H (but not the Li) are assigned to an O, forming an OH group, i.e. as imaged by FTIR spectroscopy. The shorthand notation is used in the text, and the notation designated ‘Kröger-Vink (1)’ is used in all equations, with i sites numbered in equations where necessary.

Shorthand	End-member	Kröger-Vink (1)	Kröger-Vink (2)	FTIR peak position(s), cm^{-1}
{AlH}	AlHO_2	$\{ \text{Al}_{\text{Si}}^{\cdot-} - \text{H}_i^{\cdot+} \}^{\times}$	$\{ \text{Al}_{\text{Si}}^{\cdot-} - \text{OH}_0^{\cdot+} \}^{\times}$	3316, 3377, 3430
{Al 2 H}	Al^2HO_2	$\{ \text{Al}_{\text{Si}}^{\cdot-} - ^2\text{H}_i^{\cdot+} \}^{\times}$	$\{ \text{Al}_{\text{Si}}^{\cdot-} - \text{O}^2\text{H}_0^{\cdot+} \}^{\times}$	2505, 2473
{LiOH}	LiHO	$\{ \text{Li}_i^{\cdot+} - \text{O}^{\cdot-} - \text{H}_i^{\cdot+} \}^{\times}$	$\{ \text{Li}_i^{\cdot+} - \text{O}^{\cdot-} - \text{OH}_0^{\cdot+} \}^{\times}$	3481
{LiO 2 H}	Li^2HO	$\{ \text{Li}_i^{\cdot+} - \text{O}^{\cdot-} - ^2\text{H}_i^{\cdot+} \}^{\times}$	$\{ \text{Li}_i^{\cdot+} - \text{O}^{\cdot-} - \text{O}^2\text{H}_0^{\cdot+} \}^{\times}$	2572
{Alli}	AlliO_2	$\{ \text{Al}_{\text{Si}}^{\cdot-} - \text{Li}_i^{\cdot+} \}^{\times}$		
{HOH}	H_2O	$\{ \text{H}_i^{\cdot+} - \text{O}^{\cdot-} - \text{H}_i^{\cdot+} \}^{\times}$	$\{ \text{OH}_0^{\cdot+} - \text{O}^{\cdot-} - \text{OH}_0^{\cdot+} \}^{\times}$	3475?
{Li $_2$ O}	Li_2O	$\{ 2\text{Li}_i^{\cdot+} - \text{O}^{\cdot-} \}^{\times}$		

orientation-independent relationship valid for both polarised and unpolarised light derived by Jollands *et al.* (2020a), based on the height of the 2675 cm^{-1} band from a linear baseline drawn between 2548 and 2750 cm^{-1} .

Most analyses were done using polarised light, with each profile measured twice, once with E \perp c and once with E \parallel c, giving total absorbance $\sum \text{Abs} = 2 \times \text{Abs}_{(\text{E}\perp\text{c})} + \text{Abs}_{(\text{E}\parallel\text{c})}$. Some measurements were done unpolarised, where we assume $\sum \text{Abs} \approx 4 \times \text{Abs}_{(\text{unpol})}$. The latter approximation is only valid for quartz measured on a plane including the c axis, because almost all absorbance in the OH stretching region occurs when E \perp c (e.g. Brunner *et al.*, 1961; Baron *et al.*, 2015; Potrafke *et al.*, 2019), thus, in this plane, $\text{Abs}_{(\text{unpol})} \approx 0.5 \times \text{Abs}_{(\text{E}\perp\text{c})}$. Any spectra showing clear contamination by epoxy resin were removed. The distance between the first ‘uncontaminated’ spectrum and the crystal edge was measured using a photomicrograph for each profile.

The remaining spectra were resolved into a series of pseudo-Voigt peaks, as described in the Supplementary Appendix. Then, the resolved peaks were integrated and grouped together into defect associations (Table 2) based mainly on previous work (Sibley *et al.*, 1979; Halliburton *et al.*, 1981; Kronenberg, 1994; Bachheimer, 1998; Stalder and Konzett, 2012; Baron *et al.*, 2015; Frigo *et al.*, 2016). Herein, defects are described in the text body using ‘shorthand’ notation, with curly braces (the first column of Table 2). These and other defects referred to in this study are presented in end-member and Kröger-Vink notation in Table 2. Broadly, there are two classes of defects – those that are associated with Al^{3+} replacing Si^{4+} (e.g. {AlH}, {Alli}), and those probably associated with excess O^{2-} (e.g. {LiOH}). Visualisations of the atomic structures of these defects can be found in Jollands *et al.* (2020b), their figures 4–7. The resolved peaks at 3190 , 3205 and 3296 cm^{-1} (expressed as two bands due to overlap between the former two) are assigned to a Si–O vibration (Kats, 1962). This assignment remains the subject of debate – Biró *et al.* (2016) suggests they might be related to surficial water, though this will not affect the results of this study given that neither represents structurally bound OH groups. The possibility that {HOH} is represented by a band at 3475 cm^{-1} is considered in the discussion.

LA-ICP-MS

LA-ICP-MS analyses were conducted using an Atlex 193nm laser housed inside an Australian Scientific Instruments RESOLUTION

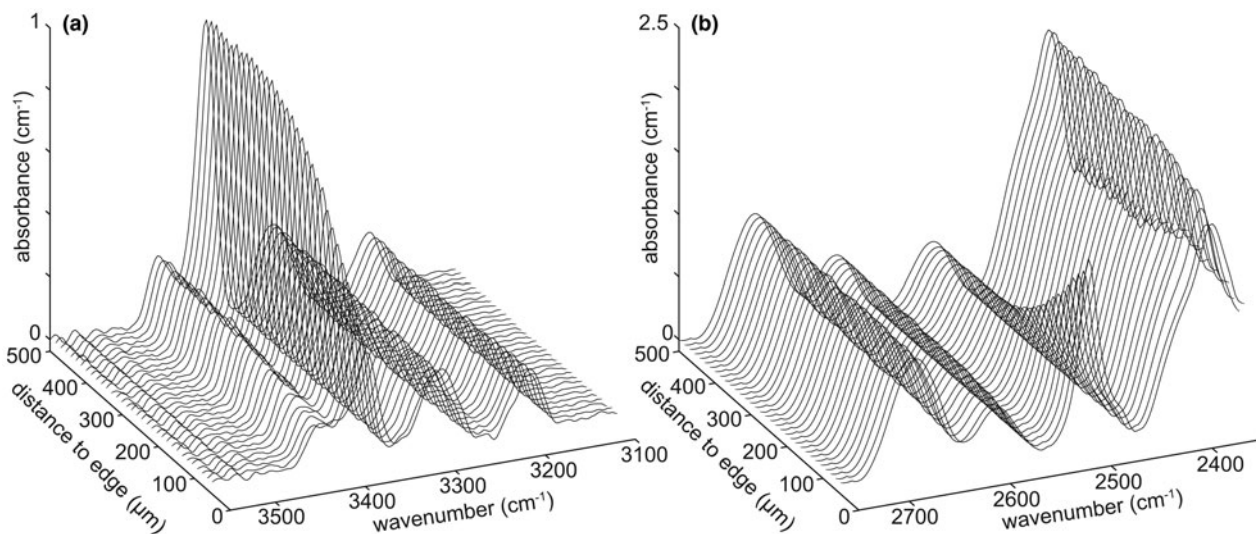


Fig. 2. Example spectra as a function of distance from the interface for the ^2H -in/ H -out experiment HQHP- H^2H . (a) Spectra from the O–H stretching region, showing H loss towards the interface. The main visible band is attributed to {AlH}. (b) Spectra from the O– ^2H stretching region, showing ^2H gain towards the interface, with considerable overlap with various Si–O overtones. The main band showing a decrease in absorbance from rim to core is attributed to {Al ^2H }. The background (core) absorbance associated with O– ^2H bonds is indistinguishable from zero – the apparent high core absorbance is due to Si–O overtones.

laser ablation system, equipped with a dual-volume Lurin Technic cell (S155), at the University of Lausanne. A 6×7 square grid of $38\ \mu\text{m}$ laser spots, with $\sim 70\ \mu\text{m}$ spacing between points, was defined, then sheared by $\sim 30^\circ$ into an approximate parallelogram, such that each spot was slightly further from the interface than the last. Analyses were done between ~ 13 – $17\ \text{J cm}^{-2}$ on-sample fluence and 30–40 Hz. The sample was ablated for 20 s, with 10–20 s background before and after each point. A standard (NIST SRM 610) was analysed after every 12 points – this was done at 10 Hz, $5\ \text{J cm}^{-2}$ fluence. ^{29}Si (internal standard), ^7Li , ^{11}B , ^{23}Na , ^{27}Al , ^{39}K and ^{49}Ti were counted for 0.01–0.1 s per sweep, giving a total sweep duration of 0.5–0.8 s. Data were processed using *Iolite* (Paton *et al.*, 2011). The first 4 s of each analysis were deleted to reduce the potential for surface contamination. Further information is provided in the Supplementary Appendix.

Results

FTIR spectra

H-in/Li-out experiments

Crystal core and rim spectra from these and all other experiments are shown in Fig. 1. As expected for a H-in experiment, spectra from the rims show consistently greater absorbance in the OH stretching region. In general, these are dominated by bands associated with {AlH}. The $3481\ \text{cm}^{-1}$ peak, attributed to {LiOH}, which is present in some of the core spectra, is consistently absent in rim spectra. The near-rim spectra of sample HQHP-TIB2 show an additional band at $3475\ \text{cm}^{-1}$, which was not present in the starting material. Both the rim and core spectra of sample HQHP-TIB6 show low absorbance of {AlH}, which is barely resolvable. There is no apparent effect of experimental pH on rim spectra, i.e. the rim spectra from experiments HQHP-pH1, -pH3, -pH5 and -pH7, all of which used the same starting material (crystal BRA3) are similar.

^2H -in/ H -out experiment

Following the initial long (53.5 hr) anneal prior to the diffusion experiment, the spectra showed only bands associated with {AlH}, with constant absorbance across the crystal (more information is provided in the Supplementary Appendix). Following the short (1 hr) diffusion experiment (HQHP- H^2H), as with the ^2H -in/ H + Li-out experiments, the interface spectrum shows a decrease, but not total loss of, absorbance in the O–H stretching region. The only O–H stretching bands in the core are the triplet associated with {AlH} (Fig. 1). At the rim, the main band associated with {Al ^2H } at $2505\ \text{cm}^{-1}$ is clearly visible. The other band of the doublet at $2473\ \text{cm}^{-1}$ is not clearly visible, but is resolvable when the spectra are fitted. Spectra from this experiment show contributions from neither {LiOH} nor {Li ^2H }.

^2H -in/ H + Li-out experiments

Crystal rim spectra (Fig. 1) show near-complete loss of absorbance in the OH stretching region relative to the core spectra. The peaks associated with {AlH} and {LiOH} are absent within the resolution of our technique (experiments DQHP-TIB6, DQHP-BRA3) or nearly so (DQHP-TIB2). This loss of absorbance in the O–H stretching region is associated with a gain in the O– ^2H stretching region. The peaks associated with O– ^2H bonds overlap with Si–O overtones, thus quantifying their absorbance requires spectra to be resolved into separate peaks, some of which are assigned to O– ^2H and others to Si–O. The {Al ^2H } defect is represented as a doublet at 2505 and $2473\ \text{cm}^{-1}$. The {Li ^2H } defect is expressed as a peak at $2572\ \text{cm}^{-1}$.

We note that the presence of these peaks associated with O– ^2H does not appear to affect the validity of the thickness correction method, even though this used a band ($2675\ \text{cm}^{-1}$) in an overlapping wavenumber region.

Profile lengths and shapes

Spectra as a function of distance from the crystal edge for two experiments are presented in Fig. 2. Profiles of defect-specific

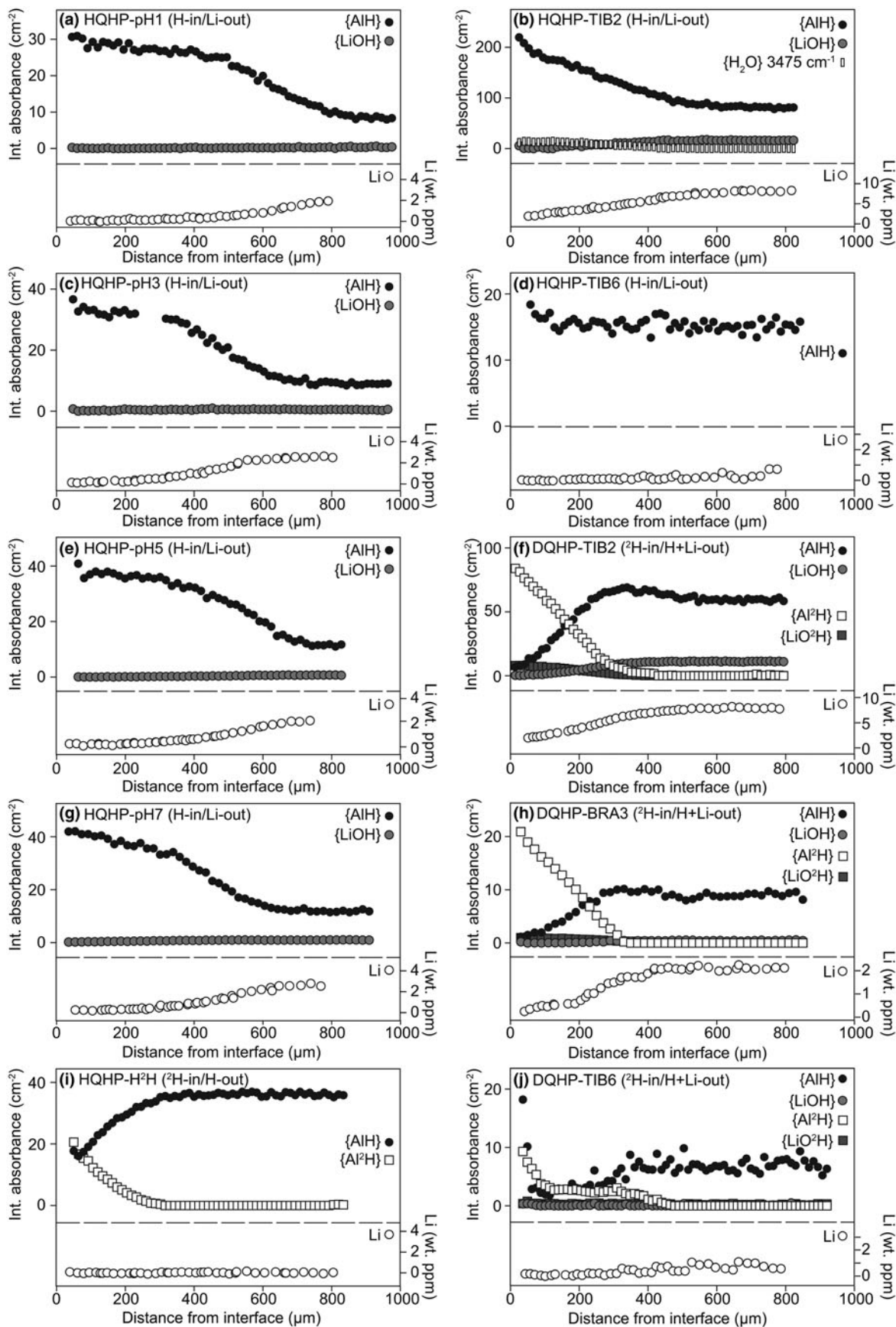


Fig. 3. FTIR profiles resolved into individual defect associations, together with the Li content measured by LA-ICP-MS. H-in/Li-out experiments are shown in panels (a)–(e) and (g), (i) shows the ²H-in/H-out experiment, and all others (f, h, j) show profiles from the ²H-in/H + Li-out experiments.

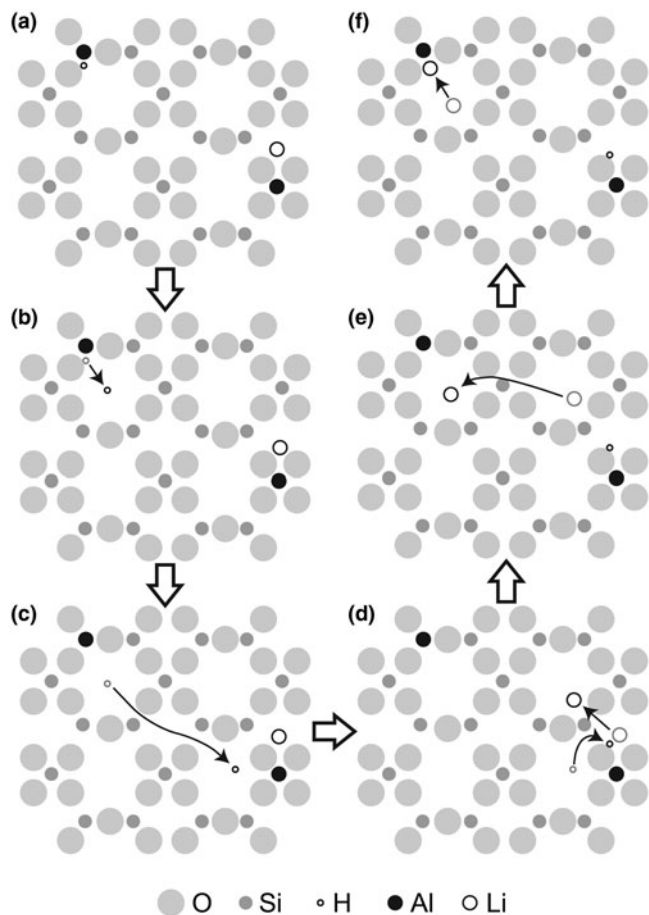


Fig. 4. Cartoon of the diffusion plus reaction concept modelled in this study. The initial condition is in (a), where one OH^- group exists adjacent to an Al^{3+} , and another Al^{3+} is charge-compensated by an interstitial Li, i.e. $\{\text{AlLi}\}$. Next, (b) the $\{\text{AlH}\}$ dissociates, thus mobilises the H. (c) The mobile H moves. The model shows it moving towards the other Al^{3+} ; this would be better represented as a random walk, possibly hopping between O ions forming the *c* axis parallel double helix. In (d) there is an exchange reaction where the mobile H displaces the immobile Li. The cartoon shows this occurring simultaneously, though this may not be the case. Image (e) is similar to (c), but with the Li now mobile. In (f), the mobile Li moves into coordination with the Al from the previously dissociated $\{\text{AlH}\}$.

absorbance (following resolution of spectra into pseudo-Voigt curves) and Li from each sample are presented in Fig. 3. For clarity, every plot in Fig. 3 is also presented in the Supplementary Appendix with expanded scales.

H-in/Li-out experiments

Profiles measured from experiments using the same starting material (BRA3) though with different pH (HQHP-pH1, -pH3, -pH5, -pH7) are similar, with no systematic variation in H concentration or profile form as a function of experimental pH. They all show $\{\text{AlH}\}$ - and $\{\text{LiOH}\}$ -versus-distance curves that do not correspond to an error-function shape (Fig. 3a, c, g, e). Rather, they show stepped shapes, with a relatively high absorbance, gently dipping section near the interface towards the core, then a sharp decrease towards background absorbance. Li profiles show the inverse trend: Li below detection limits near the rim, then an increase in Li towards the core. Whilst the effective profile lengths (600–700 μm) are not identical for the four experiments

conducted at different pH conditions, there does not appear to be any systematic relationship between profile length and pH. The absorbance–distance curve associated with the $\{\text{LiOH}\}$ defect shows a similar form to that associated with Li, albeit at much lower absorbance.

The $\{\text{AlH}\}$ profile in experiment HQHP-TIB2 (Fig. 3b) shows a gradual decrease in absorbance from rim to core, with an approximate effective diffusion distance of $\sim 600 \mu\text{m}$. However, this profile is not consistent with an error-function form, as indicated by the near linear decrease in absorbance away from the crystal edge. Again, the Li profile approximately mirrors the $\{\text{AlH}\}$ profile. The $\{\text{LiOH}\}$ profile shows a stepped shape, with relatively high absorbance in the core, then a decrease towards the rim, and a flat, low absorbance section in the $\sim 100 \mu\text{m}$ closest to the rim. The profile of the band assigned to $\{\text{HOH}\}$ mirrors that of $\{\text{LiOH}\}$ – this is the main reason for assigning the band to $\{\text{HOH}\}$. This is discussed in more detail below with regards to modelling the profiles and associated caveats.

The $\{\text{AlH}\}$ and Li profiles in experiment HQHP-TIB6 appear to be relatively flat (Fig. 3d), however the absorbance, and Li contents, are so low that it is difficult to confidently describe these profiles, so they are not discussed further.

^2H -in/H-out experiment

Profiles of absorbance versus distance of the bands attributed to $\{\text{AlH}\}$ and $\{\text{Al}^2\text{H}\}$ from experiment HQHP- ^2H show forms apparently describable as error functions (Fig. 3i), with $\{\text{AlH}\}$ showing out-diffusion and $\{\text{Al}^2\text{H}\}$ showing in-diffusion, as expected given the experimental design. A series of spectra from this experiment, showing the variation from core to rim in both the O–H and O– ^2H stretching regions, is presented in Fig. 2. The profile lengths associated with both defects are equal at $\sim 300 \mu\text{m}$, which is shorter than the profile lengths from the H-in/Li-out experiments, which were run at the same *P-T-t* conditions.

^2H -in/Li + H out experiments

These experiments consistently show profile forms and length scales that are considerably more complex than both the ^2H -in/H-out and H-in/Li-out series. The absorbance of experiment DQHP-TIB2 (Fig. 3f) is dominated by the bands attributed to $\{\text{Al}^2\text{H}\}$, which shows a near-linear decrease from rim to core in the first $\sim 250 \mu\text{m}$ of the crystal, followed by a gradual decrease from ~ 250 – $\sim 450 \mu\text{m}$ from the rim. The profile of absorbance attributed to $\{\text{AlH}\}$ generally shows out-diffusion, but with maximum absorbance at $\sim 300 \mu\text{m}$ from the rim, then a decrease in absorbance, appearing to reach background values at $\sim 600 \mu\text{m}$ from the rim. $\{\text{LiOH}\}$ and $\{\text{LiO}^2\text{H}\}$ profiles show forms approaching step shapes, and both are approximately 400 μm long. The Li profile is $\sim 500 \mu\text{m}$ long showing out-diffusion, with a concave-up form in its near rim section, and a concave down section near the core, the latter being approximately consistent with an error function.

The profiles from experiment DQHP-BRA3 (Fig. 3h) show similar relative behaviour to DQHP-TIB2, albeit at much lower absorbance. The $\{\text{AlH}\}$ profile shows a local absorbance maximum at $\sim 300 \mu\text{m}$ from the rim. The main difference in profile forms between DQHP-BRA3 and DQHP-TIB2 is that, in the former, $\{\text{Al}^2\text{H}\}$ shows a near linear decrease from the rim directly towards background values, whereas in the latter, the absorbance approached the background values gradually. As with experiment HQHP-TIB6, DQHP-TIB6 (Fig. 3j) has low H, ^2H and Li

Table 3. Results from fitting the profiles described from the H-in/Li-out experimes, and some Li-in/H-out experiments from Jollands *et al.* (2020a).

	Fixed variables			Fitted variables							
	$\Sigma i2+$	$\Sigma i1$	ΣLi (initial)	ΣLi (boundary)	$\Sigma i1 = 0.1$			$\Sigma i1 = 1$			ϵ (L cm ⁻² mol ⁻¹)
					$\log_{10}D$ (m ² s ⁻¹)	$\log_{10}K1$	χ^2_v	$\log_{10}D$ (m ² s ⁻¹)	$\log_{10}K1$	χ^2_v	
H-in/Li-out											
*HQHP-pH1	24.4	17.7	0		-8.03 (0.01)	-1.05 (0.03)	1.1	-9.03 (0.01)	-1.13 (0.03)	1.03	55,590
*HQHP-pH3	29	21.5	0		-8.18 (0.01)	-0.91 (0.04)	1.23	-9.19 (0.01)	-0.96 (0.04)	1.25	53,430
*HQHP-pH3	24.9	17.9	0		-8.17 (0.01)	-0.90 (0.03)	0.7	-9.17 (0.01)	-0.96 (0.04)	0.62	71,750
*HQHP-pH7	31.3	23	0.5		-8.05 (0.01)	-0.99 (0.04)	0.84	-9.06 (0.01)	-1.02 (0.04)	0.84	63,110
HQHP-TIB2	99	67	16		-7.55 (0.03)	-0.83 (0.05)	1.55	-8.56 (0.03)	-0.83 (0.05)	1.55	113,950
Li-in/H-out											
Q1L1	1177	266	650		-7.37 (0.02)	-0.15 (0.07)	1.07	-8.37 (0.02)	-0.15 (0.07)	1.07	32,240
Q2L1	125	69	112		-7.84 (0.08)	-0.41 (0.1)	0.63	-8.83 (0.09)	-0.42 (0.1)	0.63	64,710
Q3L1	150	93	138		-7.90 (0.03)	0.07 (0.04)	0.49	-8.9 (0.03)	0.07 (0.04)	0.49	71,430
Q4L1	92.1	55.9	90		-8.14 (0.07)	-0.13 (0.07)	1.23	-9.14 (0.07)	-0.13 (0.07)	1.23	47,140
*Q5L1	37.7	18.3	30		-8.49 (0.07)	-0.38 (0.07)	0.61	-9.49 (0.07)	-0.38 (0.07)	0.61	52,550

Numbers in parentheses represent 95% confidence intervals using the constant chi-squared boundary method (for ‘fitted variables’). If no parentheses are shown, the value has been estimated visually (‘fixed variables’). All concentrations are atomic, given per 10⁶ Si. The asterisk * denotes experiments done using the same starting material (crystal BRA3). Initial and boundary ΣLi are presented along with $\Sigma i1$ (mobile) and $\Sigma i2$ (immobile), ΣH values can be calculated from these. The ϵ values (absorption coefficients) were determined prior to fitting, assuming that the total concentration of monovalent cations remains constant along the profiles (see Supplementary Appendix). All fits were done using both $\Sigma i1 = 0.1$ and 1, for internal consistency only. χ^2_v is reduced chi-squared. K1 = equilibrium constant from equation 6.

contents with considerable scatter, such that the data cannot be described in a meaningful way. This experiment is not discussed further.

Discussion

Developing a multi-site diffusion model

In the vast majority of studies of diffusion in geologically relevant crystals using *in situ* analytical methods, profiles of trace-element concentration (C) versus distance (x) from the diffusion interface had forms corresponding to the error function (e.g. Cherniak, 2003). Such profiles can be fitted to equation 1, from which a diffusion coefficient, D, is obtained, when the time (t) is known.

$$C(x, t) = C_{core} + (C_{rim} - C_{core}) \operatorname{erfc}\left(\frac{x}{2\sqrt{Dt}}\right) \quad (1)$$

C_{rim} and C_{core} are the concentrations at the crystal rim and core, respectively and erfc is the complementary error function. This relationship assumes 1D, concentration-independent diffusion in a semi-infinite medium, plane-sheet geometry, with constant boundary conditions (Crank, 1975). In this study, the only sample showing such a profile geometry is sample DQHP-H²H, i.e. from the ²H-in/H-out experiment (Fig. 3i). This implies that, in general, it is not reasonable to describe this system using the above assumptions. However, given the experimental and analytical methods, there is no reason to assume that such geometrical and boundary conditions are inappropriate, and there is also no obvious reason to invoke concentration-dependent diffusion for H, especially at such low concentrations, and tests invoking different forms of concentration-dependent diffusion (linear and exponential) could not reproduce the observed profile shapes.

Rather, some of the profile shapes resemble diffusion coupled to inter-site reactions (Dohmen *et al.*, 2010). This describes a situation where a crystal has at least two sites on which the diffusant can sit, where each of the sites is associated with a certain diffusivity, and where it can move between the sites. Whilst this process can yield a variety of profile shapes, the most characteristic form in experiments with constant boundaries (in terms of

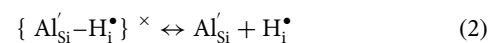
both composition and position) is the step shape (e.g. Fig. 3a, c, g, e), though various other deviations from error-function forms have also been observed (Holycross and Watson, 2017; Bloch *et al.*, 2020). This is broadly similar to the ‘trapping’ behaviour that has been well-known in metallurgy since the mid 1900s (Darken and Smith, 1949).

There is an established precedent derived from conductivity studies for invoking such a model to describe H diffusion in quartz. Kronenberg and Kirby (1987), expanding on a model proposed by Hughes (1975) and Jain and Nowick (1982) described the process as follows: “diffusion of H at high temperatures requires the dissociation of Al-H pairs to form free H_i[•] followed by transport to neighboring Al_{Si}⁺ sites”, referring to the {AlH} defect, the major defect in most natural and some synthetic quartz (e.g. Halliburton *et al.*, 1981; Müller and Koch-Müller, 2018; Tollan *et al.*, 2019). The implication is that the overall mobility of H should be a function of: (1) the rate at which free H can hop through the lattice; and (2) a constant describing dissociation of charge-neutral associations. This is expanded on below, considering each type of experiment in turn. Further information regarding all models, including curve fitting, is provided in the Supplementary Appendix.

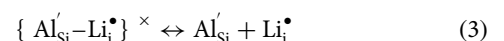
H-in/Li-out experiments

For these experiments, we first consider that H moves by dissociation of H_i[•] (or ²H_i[•], Li_i[•]) from its charge-balancing ion (Al_{Si}⁺), followed by hopping to a nearby position. The process is illustrated in cartoon form in Fig. 4.

The dissociation of the {AlH} defect, which dominates the FTIR spectra (Figs 1 and 3) will be described by equation 2, where the H is described generically as ‘interstitial’ with an i:



A similar reaction should be possible for Li:



These reactions are equivalent to, for example, eqs. 1b and 1a, respectively, in Campone *et al.* (1995) and eq. 1 of Jain and

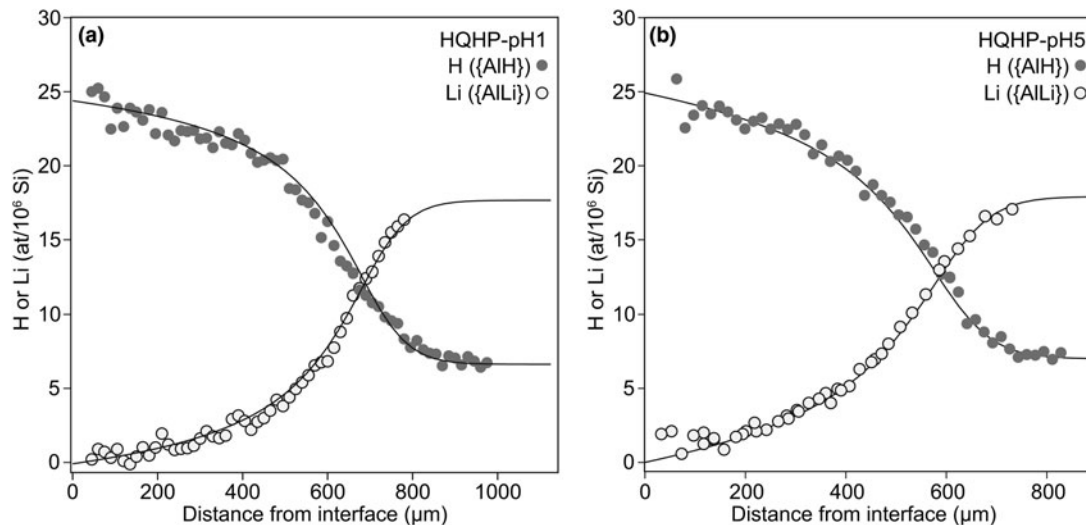


Fig. 5. Profiles of {AlH} and {ALi} from experiments (a) HQHP-pH1 and (b) HQHP-pH5, fitted. The measured Li content is corrected to account for the {LiOH} defect. Model parameters: total time = 3600 s, $\Delta x = 25 \mu\text{m}$. Initial and boundary conditions: (a) $\Sigma i1$ (mobile) + $\Sigma i2$ (immobile, Al-associated) = $24.4 / 10^6 \text{Si}$; ΣLi (initial) = $17.9 / 10^6 \text{Si}$; ΣLi (boundary) = $0 / 10^6 \text{Si}$. (b) $\Sigma i1$ (mobile) + $\Sigma i2$ (immobile, Al-associated) = $24.9 / 10^6 \text{Si}$; ΣLi (initial) = $17.9 / 10^6 \text{Si}$; ΣLi (boundary) = $0 / 10^6 \text{Si}$. All other fit parameters (D , K , χ_v^2 , ϵ) are provided in Table 3. Fits to data from other experiments are provided in the Supplementary Appendix.

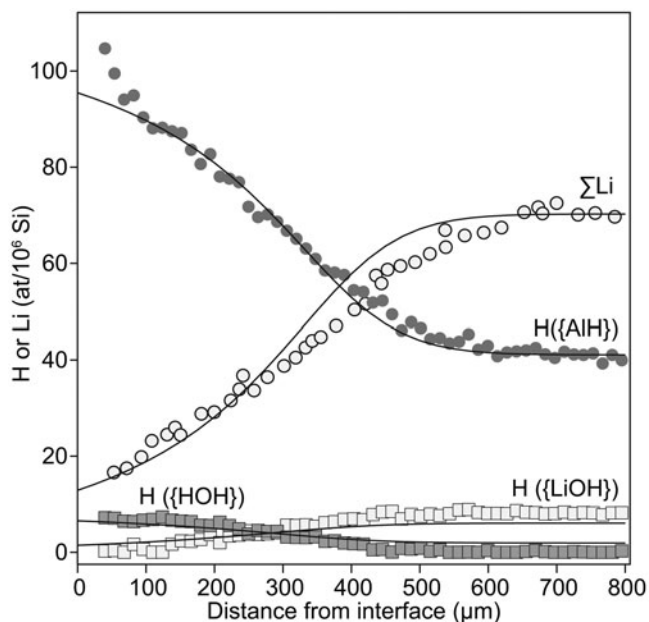


Fig. 6. The profile from experiment HQHP-TIB2, resolved, with the {AlH}, {LiOH}, {HOH} (assumed to be represented by a band at 3475cm^{-1}) and ΣLi modelled simultaneously. This fit was done manually, i.e. no non-linear least-squares regression was attempted, so is not guaranteed to be the best fit. Model parameters: $\Delta x = 25 \mu\text{m}$, total time = 3600 s, $\log_{10} D$ ($\text{m}^2 \text{s}^{-1}$) = -9 ; $\Sigma i1$ (mobile) = $2 / 10^6 \text{Si}$; $\Sigma i2$ (immobile, Al-associated) = $105 / 10^6 \text{Si}$; $\Sigma i3$ (immobile, O-associated) = $8 / 10^6 \text{Si}$; $K1 = 0.1$; $K2 = 0.2$.

Nowick (1982). That the H and Li are both given subscript i should not be taken to suggest that they occupy the same interstitial site: $\{\text{Al}'_{\text{Si}}-\text{H}_i^{\bullet}\}^{\times}$ can also be written (more correctly) as $\{\text{Al}'_{\text{Si}}-\text{OH}_i^{\bullet}\}^{\times}$, for example, and the Li probably occupies the large open channel parallel to the c axis.

For simplicity, we assume that in a simple H-Li exchange, it should be possible to combine the two reactions, upon which the Al'_{Si} cancel out. In order to distinguish between the H or Li in 'interstitial' sites associated with Al (immobile), and those in

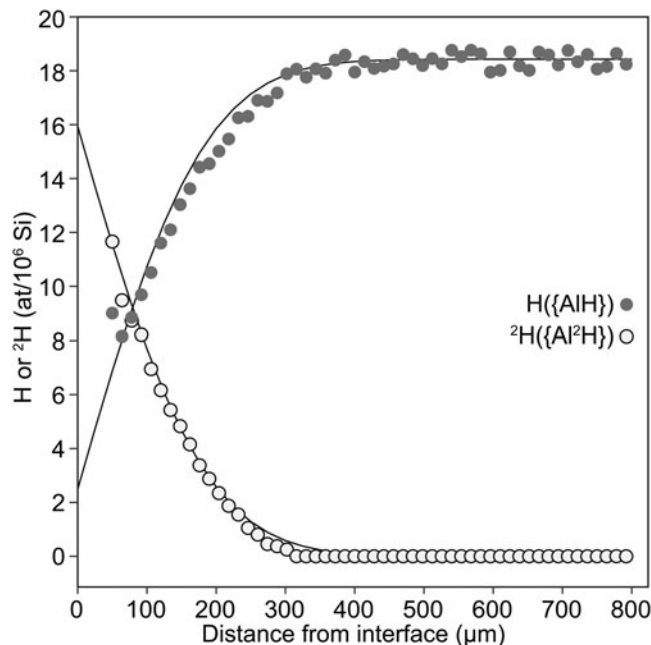
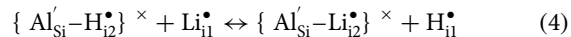


Fig. 7. Models (solid lines) representing the ^2H -in/H-out experiment, together with data (circles) from experiment HQHP-H ^2H . The model parameters are provided in Table 4. Model parameters (for other model parameters, see Table 4): $\Sigma i1$ (mobile) + $\Sigma i2$ (immobile, Al-associated) = $18.5 / 10^6 \text{Si}$; ΣH (initial) = $0 / 10^6 \text{Si}$; ΣH (boundary) = $16 / 10^6 \text{Si}$.

a dissociated, mobile configuration, we use 'i2' and 'i1' for the former and latter, respectively. Herein, 'i1' always refers to an interstitial site where the occupying ion is free to move. Therefore, combining equations 2 and 3, and adding this notation, we have:



which describes the dissociation of {ALi} and {AlH}, forming two mobile ions that swap places forming two new immobile defects.

Table 4. Results from fitting the profiles described from the ^2H -in/H-out experiment.

	Fixed variables				Fitted variables			
	$\sum i2 + \sum i1$	$\sum ^2\text{H}$ (initial)	$\sum ^2\text{H}$ (boundary)	$\text{Log}_{10}\text{K3}$	$\sum i1 = 0.1$		$\sum i1 = 1$	
					$\log_{10}D$ ($\text{m}^2 \text{s}^{-1}$)	χ^2_v	$\log_{10}D$ ($\text{m}^2 \text{s}^{-1}$)	χ^2_v
*DQHP-H 2 H	18.5	0	16	0	-9.28 (0.03)	0.89	-10.28 (0.03)	0.89

See Table 3 for notation details. K3 = equilibrium constant from equation 14. In this case K3 was set to 1. Again, fits were done with both $\sum i1 = 0.1$ and 1

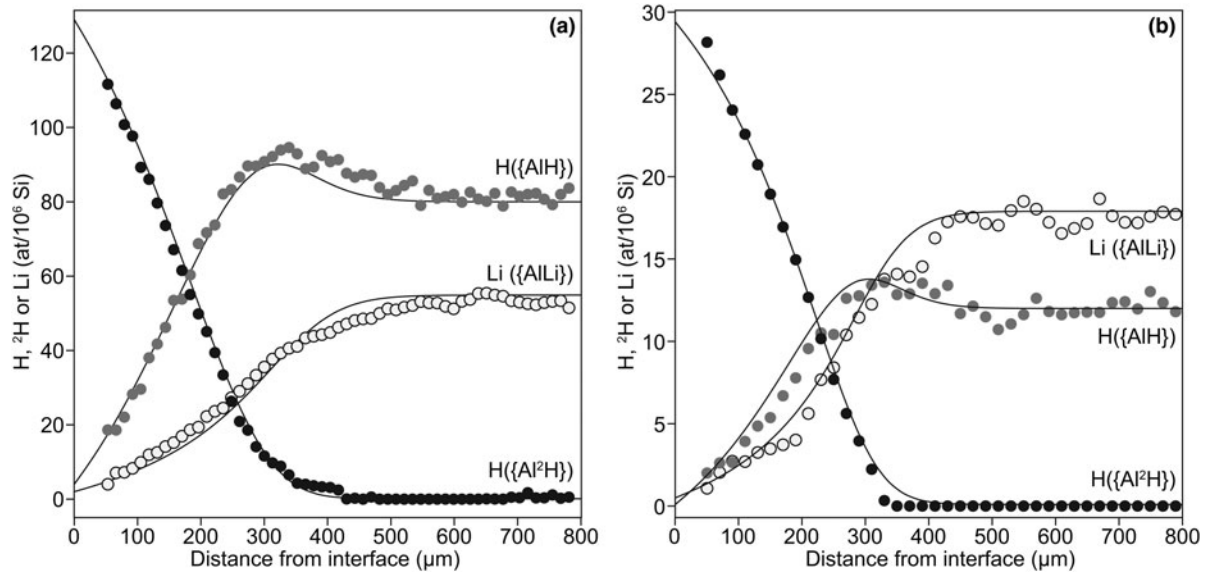
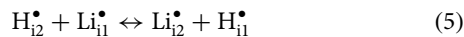


Fig. 8. Models (solid lines), along with data (circles) from ^2H -in/H + Li out experiments DQHP-TIB2 (a) and DQHP-BRA3 (b). The models were matched to the data visually (i.e. no non-linear least-squares regression). The models include neither $\{\text{LiOH}\}$ nor $\{\text{HOH}\}$ defects. Note that both models reproduce the observed hump in $\text{H}(\{\text{AlH}\})$ at $\sim 300 \mu\text{m}$ from the interface without requiring uphill diffusion. Note also that the tracer diffusivities of H, Li and ^2H are assumed to be equal for simplicity. Both models: $\Delta x = 25 \mu\text{m}$; total time = 3600 s. Initial and boundary conditions (other model parameters presented in Table 5): (a) $\sum i1$ (mobile) = $1 / 10^6 \text{Si}$; $\sum i2$ (immobile, Al-associated) = $134 / 10^6 \text{Si}$; $\sum \text{Li}$ (initial) = $54.9 / 10^6 \text{Si}$; $\sum \text{Li}$ (boundary) = $2 / 10^6 \text{Si}$; $\sum \text{H}$ (initial) = $80 / 10^6 \text{Si}$; $\sum \text{H}$ (boundary) = $4 / 10^6 \text{Si}$, (b) $\sum i1$ (mobile) = $1 / 10^6 \text{Si}$; $\sum i2$ (immobile, Al-associated) = $29 / 10^6 \text{Si}$; $\sum \text{Li}$ (initial) = $17.9 / 10^6 \text{Si}$; $\sum \text{Li}$ (boundary) = $0.5 / 10^6 \text{Si}$; $\sum \text{H}$ (initial) = $12 / 10^6 \text{Si}$; $\sum \text{H}$ (boundary) = $0.1 / 10^6 \text{Si}$.

For the purposes of modelling, this is again simplified by removing the Al to give equation 5:



The method for modelling this process is described briefly here, with further details, including fitting routines, estimations of uncertainties, model limitations, etc., in the Supplementary Appendix. The method involves dividing the total model time into a series of small steps, i.e. the explicit finite difference method. Each time step comprises a diffusion step ($\Delta x = 25 \mu\text{m}$, Δt adjusted to maintain numerical stability), where the mobile H and Li diffuse (diffusion only on the i1 site, i.e. only Li_{i1}^{\bullet} and H_{i1}^{\bullet}), assuming that a single diffusion coefficient can describe both H and Li, then a reaction step where the reaction in equation 5 is modelled. This is done using the equilibrium expression (herein K1 for the reaction in equation 5) specified, using square brackets for concentration (now using units of atoms per 10^6Si):

$$\text{K1} = \frac{[\text{H}_{i1}^{\bullet}][\text{Li}_{i2}^{\bullet}]}{[\text{Li}_{i1}^{\bullet}][\text{H}_{i2}^{\bullet}]} \quad (6)$$

and with various constraints of mass balance and site balance

imposed:

$$\sum i1 = [\text{Li}_{i1}^{\bullet}] + [\text{H}_{i1}^{\bullet}] \quad (7)$$

$$\sum i2 = [\text{Li}_{i2}^{\bullet}] + [\text{H}_{i2}^{\bullet}] \quad (8)$$

$$\sum \text{H} = [\text{H}_{i1}^{\bullet}] + [\text{H}_{i2}^{\bullet}] \quad (9)$$

$$\sum \text{Li} = [\text{Li}_{i1}^{\bullet}] + [\text{Li}_{i2}^{\bullet}] \quad (10)$$

Solving these equations yields the concentrations of Li_{i1}^{\bullet} , H_{i1}^{\bullet} , Li_{i2}^{\bullet} and H_{i2}^{\bullet} , which is possible if four of K1, $\sum i1$, $\sum i2$, $\sum \text{H}$ and $\sum \text{Li}$ are known (further information in the Supplementary Appendix). After the reaction step, diffusion occurs again, then reaction, and so on, until the total model time is reached. The final model output is a series of curves representing the concentration of each defect as a function of distance from the boundary, which are then fitted to the data using non-linear least-squares regression. Uncertainties (95% confidence intervals) for the fitted

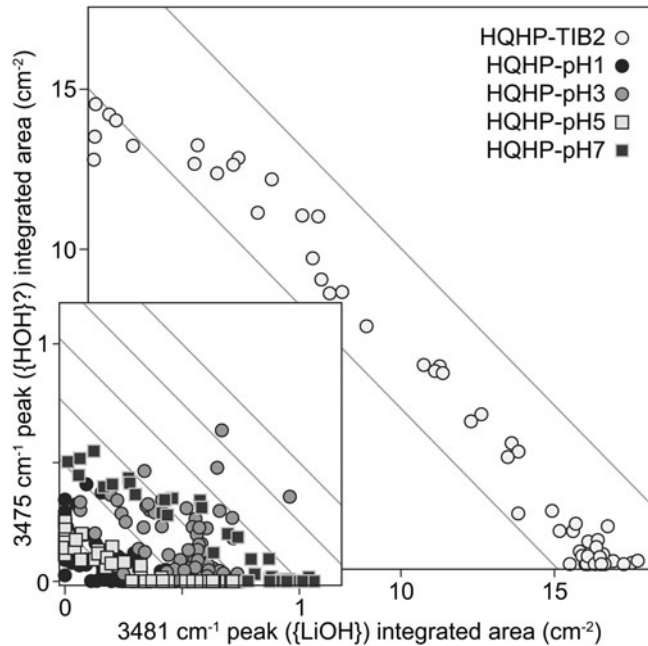


Fig. 9. The integrated areas of the peak assigned to {LiOH} ($\sim 3481\text{ cm}^{-1}$) versus those of the peak at $\sim 3475\text{ cm}^{-1}$, for experiments HQHP-pH1, HQHP-pH3, HQHP-pH5, HQHP-pH7 and HQHP-TIB2. Grey lines have a slope of -1 , and are provided as a visual guide only.

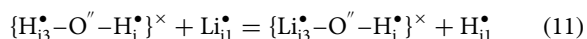
model parameters, $K1$ and D , were determined using the constant chi-squared boundary method (Press *et al.*, 2007). The initial and boundary concentrations of $\sum Li$, $\sum i1$ and $\sum i2$ were set manually for each experiment. The best fit parameters and uncertainties are presented in Table 3 for the five H-in/Li-out experiments modelled in this way. The $\sum i1$ parameter is problematic, as we have no independent constraints on its value, so, for internal consistency only, this was set to either 0.1 or 1 atoms/ 10^6 Si. This is discussed further below with regards to model caveats.

Model fits for profiles from two H-in/Li-out experiments are presented in Fig. 5, showing that the model successfully reproduces the forms and lengths of the profiles.

{AlH} and {LiOH} defects in H-in/Li-out experiments

A limitation of the model development above is that it did not consider the {LiOH} defects that are visible in the FTIR spectra of most experiments as a band at $\sim 3481\text{ cm}^{-1}$ (e.g. Baron *et al.*, 2015; Frigo *et al.*, 2016). Adding this defect adds considerable complexity and is only treated briefly here (a detailed description is provided in the Supplementary Appendix), and non-linear least-squares regressions were not attempted – all fitting was done visually only.

As with the reactions presented above, we assume that {LiOH} can dissociate, forming a mobile H or a mobile Li. If we assume that there exists also a {HOH} defect, then we have:



now denoting one of the interstitial sites as $i3$, and keeping the mobile interstitial site as $i1$. As another simplifying assumption, the other i site is assumed to not be involved in the reaction, and is left as i . It is of course possible that there also exists a reaction involving a defect with Li_2O stoichiometry, however this possibility is not considered. Now, adding the reaction in equation 11

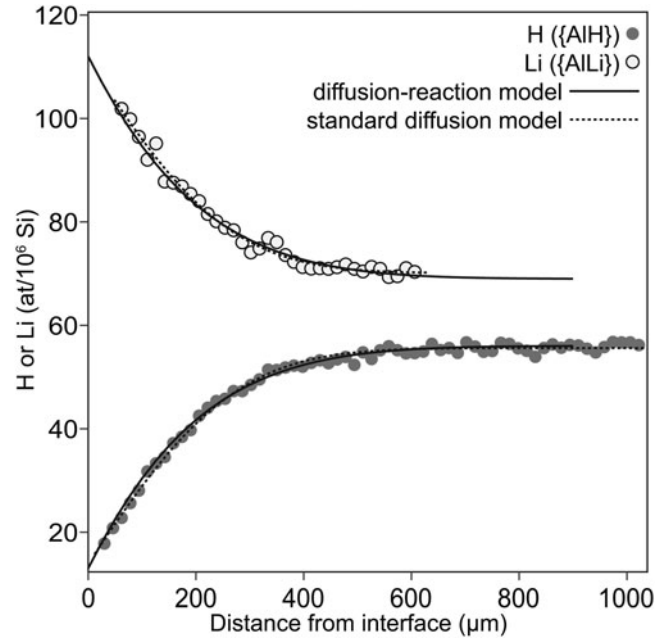


Fig. 10. H and Li profiles from a Li-in/H-out experiment (Q2L1 of Jollands *et al.*, 2020a), fitted using the diffusion–reaction model (solid line). The model parameters are presented in Table 3. Also shown (dashed lines) are fits with error-function forms, barely discernible from the diffusion–reaction model curves, i.e. equation 1. Other fits are available in the Supplementary Appendix.

into the reaction step in the diffusion–reaction model (the equilibrium constant for this reaction is herein denoted $K2$):

$$K2 = \frac{[H_{i1}^{\bullet}][Li_{i3}^{\bullet}]}{[Li_{i1}^{\bullet}][H_{i3}^{\bullet}]} \quad (12)$$

and assuming that the free H_i^{\bullet} and Li_i^{\bullet} can move between defects associated with O'' and Al_{Si}' , profiles for {LiOH}, {HOH}, {AlH} and {AlLi} are generated simultaneously.

An example model output is shown in Fig. 6 along with the data from experiment HQHP-TIB2. Modelling results show that the two Li-bearing defects {LiOH} and {AlLi} show out-diffusion, where {HOH} and {AlH} show in-diffusion profiles. One short-coming of the model is that it requires a {HOH} defect, however such a defect is not definitively known in the FTIR spectra of quartz – this is discussed further below with other model caveats.

²H-in/H-out experiment

The profiles from this experiment appear to show error-function forms (Fig. 3i), which might be considered as consistent with simple concentration-dependent diffusion, i.e. equation 1. However, if one assumes that H–Li exchange requires a diffusion–reaction model then there is no obvious reason that this should not also be the case for H–²H exchange. Therefore, a diffusion–reaction model was constructed based on equation 13, i.e. the ²H equivalent of equation 4:



where, as before, ‘ $i1$ ’ represents a mobile position, and ‘ $i2$ ’ is immobile. We assume that the equilibrium constant for this reaction (herein $K3$) can be approximated as 1, at least within the

Table 5. Results from approximate visual fitting of two ^2H -in/H + Li out experiments.

					Fixed variables				
	$\sum i1$	$\sum i2$	$\sum \text{Li}$ (initial)	$\sum \text{Li}$ (boundary)	$\sum \text{H}$ (initial)	$\sum \text{H}$ (boundary)	$\log_{10} D$ (m^2s^{-1})	$\log_{10} K1$	$\log_{10} K3$
DQHP-TIB2	1	134	54.9	2	80	4	-9.1	-1.05	0
*DQHP-BRA3	1	29	17.9	0.5	12	0.1	-9.7	-0.92	0

See Table 3 for notation details. K1 and K3 are the equilibrium constants from equations 6 and 14, respectively. These fits were done only with $\sum i1 = 1$.

limitations of our experimental and analytical methods:

$$K3 = \frac{[\text{H}_{i2}^*][^2\text{H}_{i1}^*]}{[^2\text{H}_{i2}^*][\text{H}_{i1}^*]} \approx 1 \quad (14)$$

The profile from this experiment was then modelled and fitted, as above, with H contents (as H_2O) determined using $\epsilon = 89,000 \text{ L cm}^{-2} \text{ mol}^{-1}$ (Thomas *et al.*, 2009), and ^2H contents using $\epsilon = 79,700 \text{ L cm}^{-2} \text{ mol}^{-1}$. The derivation of the ϵ value for $^2\text{H}_2\text{O}$ is described in full in the Supplementary Appendix, however, simply, ϵ for $^2\text{H}_2\text{O}$ is adjusted to minimise the variance of $^2\text{H} + \text{H}$ (atomic basis) for all points along the whole profile, whilst keeping ϵ for H_2O constant. The assumption is that $^2\text{H} + \text{H}$ should be constant along the profile in the ^2H -in/H-out experiment, i.e. every ^2H gained is compensated by one H being lost.

When K is set to 1, the modelled profiles approach error-function shapes, as we observe in the ^2H -in/H-out experiment. It appears to be possible to generate error-function forms that fit the data with any positive value of $\sum i1$ (total mobile $\text{H} + ^2\text{H}$) up to the total value of $\text{H} + ^2\text{H}$. As $\sum i1$ decreases, D increases, and where $\sum i1 = \text{H} + ^2\text{H} \approx 18.5 / 10^6 \text{ Si}$ (the total $\text{H} + ^2\text{H}$ is set to 18.5 atoms per 10^6 Si , see Fig. 7, Table 4), D equals that determined by fitting the data to equation 1.

However, the starting material for the ^2H -in/H-out experiment prior to the initial equilibration step was the same as that used for the ‘pH series’ (HQHP-pH1, -pH3, -pH5 and -pH7, crystal BRA3). The stepped profiles from the latter series could not be well fitted with $\sum i1$ over $\sim 3\text{--}5 / 10^6 \text{ Si}$ – further information is provided in the Supplementary Appendix. If we then consider the results of internally consistent fitting of both the ‘pH series’ and this HQHP- ^2H experiment, the diffusion coefficient associated with ^2H -H exchange is around one order of magnitude slower than that of H-Li exchange. This is not intuitively reasonable if we assume that diffusivity should increase with decreasing mass and ionic radius of the diffusant, but has been observed before – for example, the monovalent cation with the highest measured diffusivity in diffusion experiments to date is Na (Frischat, 1970). However, we note that Frischat (1970) used very different experimental methods (little information is provided, however assuming the methods are similar to Frischat (1968)) – radioactive ^{22}Na was diffused into quartz from a film of $^{22}\text{NaCl}$ at atmospheric pressure, then ^{22}Na vs. depth profiles were measured using serial grinding and by measuring the residual activity.

Overall, we can therefore state that whilst the results of the ^2H -in/H-out experiment do not require a diffusion-reaction model, a diffusion-reaction model can reproduce the approximately error function profile shapes.

^2H -in/Li + H out experiments

Modelling these experiments is considerably more challenging than the H-in/Li-out or ^2H -in/H-out experiments, given that

there are now (at least) six unknowns to be solved for in the reaction step, being the concentrations of $\{\text{AlH}\}$, $\{\text{Al}^2\text{H}\}$, $\{\text{AlLi}\}$ plus the mobile Li, H and ^2H (i.e. those in the ‘i1’ positions). This is already an incomplete description – ideally we should have more unknowns, i.e. the above plus $\{\text{LiOH}\}$, $\{\text{HOH}\}$ and $\{^2\text{HOH}\}$ (and potentially $\{\text{Li}_2\text{O}\}$). Taking the simplified system, i.e. ignoring the O-associated defects, there is no analytical solution to the simultaneous equations in the reaction step, meaning that the equations have to be solved numerically. For this reason, as with the model presented above including the Al- and O-associated defects, the measured profiles from these experiments were not fitted by non-linear least-squares regression. Instead, the profiles of $\{\text{AlH}\}$, $\{\text{Al}^2\text{H}\}$ and $\{\text{AlLi}\}$ from two experiments were visually fitted only by adjusting the initial and boundary concentrations of Li and H, $\sum i1$, $\sum i2$ and D .

Models are presented in Fig. 8, taking $K1 = 0.1$ (H-Li exchange, equation 4) and $K3 = 1$ (H- ^2H exchange, equation 13) which are broadly consistent with the model outputs presented above. These models generate profiles with several interesting features. Firstly, the $\{\text{AlH}\}$ profiles show maxima at $\sim 300 \mu\text{m}$ from the crystal edge, where we would normally expect the maxima to be in the crystal cores. Secondly, the near-interface out-diffusion section of the $\{\text{AlH}\}$ profile is concave-up, which is broadly the opposite of the error-function profile form. Thirdly, the $\{\text{Al}^2\text{H}\}$ profile is concave-down near the interface, again the opposite of the error-function form. All of these model outputs are consistent with the data.

Of particular note are the local maxima in $\{\text{AlH}\}$ profiles. Such features would generally be described as ‘uphill-diffusion’, i.e. diffusion of an element against its own concentration gradient, which is not uncommon in multi-component diffusion systems (Zhang, 2010). In this case, all modelled diffusion is downhill – the maxima are due to the presence of a reaction step in the model rather than uphill diffusion. Even though non-linear least-squares regression was not used (the profiles were matched to models by visual estimations only), these results provide clear support to the use of the diffusion-reaction model. They also support the use of such a model for the ^2H -in/H-out experiments presented above, despite the model not being required for an adequate fit.

Model caveats and shortcomings

Whilst the model presented above is successful at fitting the results of different experiments with general internal consistency, there are several caveats, limitations and simplifying assumptions that warrant further discussion.

First, in equation 5, and then throughout, it was implicitly assumed that two dissociation and association reactions occur simultaneously. This is not physically realistic – the two reactions would ideally be modelled separately.

Second, and probably the most problematic shortcoming of this model is that it requires free H_{i1}^* and Li_{i1}^* to be invoked, the former not being associated with any known band in FTIR spectra of quartz. This means that the model needs to assume some concentration of $H_{i1}^* + Li_{i1}^*$, i.e. the sum concentration of the mobile cations at any given time ($\sum i1$, equation 7). The power of FTIR spectroscopy in being able to distinguish different point defects is somewhat inconvenient here – we would probably not be considering this caveat if only the total H content, rather than full FTIR spectra had been measured. In this study, all profiles were fitted with $\sum i1$ set to both 0.1 and 1 atoms per 10^6 Si for internal consistency. Some profiles could be well fitted with much lower or higher values of $\sum i1$ however 0.1 and 1 atoms per 10^6 Si allowed all profiles to be fitted – further information is provided in the Supplementary Appendix. In lieu of any obvious better alternative, we also made the assumption that these mobile cations (H_{i1}^* and Li_{i1}^*) move into their immobile states ($\{AlH\}$ and $\{AlLi\}$) at the end of the experiment, i.e. they move from ‘i1’ to ‘i2’ sites on quench.

Third, in all models, we assume that a single diffusion coefficient is sufficient along the ‘i1’ pathway. There is, however, no reason to assume that (for example) the diffusion coefficient of Li is equal to that of H. By making this assumption, we are effectively applying a H–Li inter-diffusion coefficient, although it is not stated as such (see eq. 5 of Stalder (2021) and the associated text for a discussion of this concept). Again, this is done for simplification – if we considered this as inter-diffusion, we would need two ‘tracer’ diffusion coefficients, one for Li and one for H (three for the 2H -in/H + Li out experiments), and D would be concentration-dependent, i.e. different at every point along the profile. At this stage of model development, the aim is to minimise the number of variables. It is likely, however, that the uncertainties related to D due to this model limitation are minor relative to those related to the unconstrained nature of $\sum i1$ (second point, above).

Fourth, in modelling the HQHP-TIB2 profile, a $\{HOH\}$ defect was assumed – this was represented by a band at $\sim 3475\text{ cm}^{-1}$, which has not been assigned to this defect. The main reason was that the absorbance of this band appears to be inversely proportional to that of the 3481 cm^{-1} $\{LiOH\}$ band (Fig. 9). Some arguments for and against this attribution are presented in the following paragraph.

The 3475 cm^{-1} band was present, although barely resolvable, in experiments HQHP-pH1, -pH3, -pH5 and -pH7. Additionally, polarised FTIR spectra show that the total absorbance of this band is entirely dominated by its E_{⊥c} contribution (see the Supplementary Appendix), as with most bands in the OH stretching region of quartz – this means that if the band represents a defect with H₂O stoichiometry, it almost certainly includes structurally-bound OH. Jollands *et al.* (2020b) predicted that a defect with H₂O stoichiometry should have bands at 3411 and 3498 cm^{-1} , with the latter showing most absorbance with E_{⊥c}, which would be broadly consistent with our suggestion, though there is no evidence for the former band (although it would probably be subsumed by the $\{AlH\}$ bands, if it were present). Additionally, Kats (1962) suggested that a band at 3470 cm^{-1} was not associated with any cation other than H⁺ (summarised by Kronenberg *et al.*, 1986). However, it was not observed in quartz crystals grown in the pure SiO₂–H₂O system (Stalder and Konzett, 2012).

Fifth, we have assumed that the equilibrium constants K1, K2 and K3 can be assumed to be constant along the profiles. This is unlikely to be exactly correct, however the ability to fit different

profile forms using single equilibrium constants suggests that this effect is minor relative to the other caveats.

The effect of pH

No effect of experimental pH was observed, in terms of either interface H and Li contents, or diffusion profile length/geometry. The original motivation for conducting experiments at different pH conditions was to determine whether a different activity of protons in the fluid would change the interface H/Li ratio, which may then affect the profile length and shape. That no effect of pH was observed does not mean that no effect is possible, however it could be explained by the fact that (1) the difference in pH is considerably lower at experimental conditions than at room temperature or (2) the total amount of Li and H that can be incorporated into the crystals is so low, given the low Al content, that any small variations in Li and H concentration might not be resolvable. Experiments conducted at conditions where the relative pH differences are larger (i.e. at higher pressure) could be enlightening, as could experiments using quartz crystals with higher Al contents.

Reconciling observations from H-in and H-out experiments?

One peculiar observation is that our previous experiments considering H–Li exchange through Li-in/H-out diffusion (Jollands *et al.*, 2020a) gave results that appear to be inconsistent with those presented in this study. Where the H-in/Li-out experiments in this study generally yielded H concentration profiles with complex shapes, those in the Li-in/H-out experiments showed shapes that were, within uncertainty, consistent with error-function forms (Jollands *et al.*, 2020a).

In fact, if the flux in the diffusion–reaction model is reversed, i.e. such that the boundary conditions of Li and H lead to Li in-diffusion, but all other parameters (K , D , number of sites) are kept constant, profile forms close to error functions are the result. To illustrate this further, the Li and $\{AlH\}$ profiles from the 807°C, Li-in/H-out experiments of Jollands *et al.* (2020a) (their Q1L1, Q2L1, Q3L1, Q4L1 and Q5L1) were re-fitted using the diffusion–reaction model. With $\sum i1 = 1/10^6\text{Si}$, we obtain $\log_{10}D$ ($\text{m}^2\text{ s}^{-1}$) ≈ -8.5 to -9.5 , and $\log_{10}K1 = -0.4$ to 0.1 (Table 3), and the profiles from the previous study were fitted satisfactorily (Fig. 10, and Supplementary Appendix). Fitting the same profiles to a standard error-function solution to Fick’s second law gives $\log_{10}D$ ($\text{m}^2\text{ s}^{-1}$) between -11.1 to -11.8 (see Supplementary dataset 1 of Jollands *et al.*, 2020a for original fit parameters), i.e. 2–3 orders of magnitude lower than that obtained by using the diffusion–reaction model. Another observation of the Jollands *et al.* (2020a) investigation was a relatively large spread in measured D at any given temperature – approximately ± 0.3 orders of magnitude around the mean. It is likely that this was due to the use of a variety of different starting materials, however there was no clear systematics observed. Alternatively, this spread in D might relate to the application of a simple diffusion model to a system where a more complex diffusion–reaction model is warranted. However, attempts to re-fit all data from the previous study using the new model were unsuccessful in this regard, the difference between D becomes larger – this almost certainly relates to the fact that we have little or no constraint on the elusive $\sum i1$ parameter, either in terms of absolute value or relative values between different starting materials.

The original objective of the Jollands *et al.* (2020a) investigation was to provide diffusion coefficients that could be applied to Li-in/H-out profiles observed previously in some volcanic quartz crystals (Charlier *et al.*, 2012; Tollan *et al.*, 2019). Whilst it now appears that the simple diffusion model applied by Jollands *et al.* (2020a) was not strictly appropriate (we previously used equation 1), it is reasonable to assume that their phenomenological diffusion coefficients are appropriate for use as a diffusion chronometer, at least within their quoted uncertainties. This is because the compositional range of their starting materials (in terms of H and Li concentrations) straddled the composition of their studied volcanic quartz, from the Bishop Tuff. Regardless of our above discussion and the considerable complexities in this system, we would still propose that simple solutions or numerical approximations of Fick's second law, such as in equation 1, coupled with the phenomenological Jollands *et al.* (2020a) diffusion coefficients are appropriate for purposes of H diffusion chronometry using volcanic quartz in situations where H is lost and Li gained, at least within any reasonable uncertainty.

Conclusion

On the basis of a series of diffusion experiments and *in situ* analyses, this study demonstrates that H, ^2H and Li diffusion in quartz involves a process where H and other monovalent cations move by dissociating from a charge-compensating species, generally Al^{3+} , then moving rapidly to another charge-balancing site, where they become immobilised. Models invoking this process can create different profile forms consistent with experimental observations: step shapes in H-in/Li-out experiments, localised humps in ^2H -in/Li+H out experiments, and error-function forms in Li-in/H-out and ^2H -in/H-out experiments. Models describing this complex diffusion mechanism of H in quartz have been proposed previously (e.g. Kronenberg and Kirby, 1987) – this study provides independent support.

Supplementary material. All FTIR spectra and LA-ICP-MS data are available at <https://doi.org/10.17632/v3p5fw65bv.1>. To view the Supplementary Appendix for this article, please visit <https://doi.org/10.1180/mgm.2021.105>

Acknowledgements. Jörg Hermann is thanked for access to the FTIR lab at the University of Bern. Alexey Ulianov is thanked for maintaining the LA-ICP-MS at the University of Lausanne in such a condition that the quartz analyses at ablation conditions that were extreme for our instrument, were straightforward. Various people have been involved to some extent in establishment, use and upkeep of the hydrothermal equipment at the University of Lausanne: Tom Sisson, Romain Lafay, Mattia Pistone, Eli Bloch – their work facilitated these experiments. Thanks to Roland Stalder and two anonymous reviewers for their comments that helped to improve the manuscript. This work was supported by the University of Lausanne and a grant from the Swiss National Science Foundation (P400P2_183872) to MCJ.

References

- Aines R.D. and Rossman G.R. (1984) Water in minerals? A peak in the infrared. *Journal of Geophysical Research: Solid Earth*, **89**, 4059–4071.
- Bachheimer J.P. (1998) An investigation into hydrogen stability in synthetic, natural and air-swept synthetic quartz in air temperatures up to 1100°C. *Journal of Physics and Chemistry of Solids*, **59**, 831–840.
- Baron M.A., Stalder R., Konzett J. and Hauenberger C.A. (2015) OH-point defects in quartz in B- and Li-bearing systems and their application to pegmatites. *Physics and Chemistry of Minerals*, **42**, 53–62.
- Biró T., Kovács I.J., Király E., Falus G., Karátson D., Bendő Z., Fancsik T. and Sándorné J.K. (2016) Concentration of hydroxyl defects in quartz from various rhyolitic ignimbrite horizons: Results from unpolarized micro-FTIR analyses on unoriented phenocryst fragments. *European Journal of Mineralogy*, **28**, 313–327.
- Bloch E., Jollands M., Devoir A., Bouvier A., Ibañez-Mejía M. and Baumgartner L.P. (2020) Multispecies diffusion of yttrium, rare earth elements and hafnium in garnet. *Journal of Petrology*.
- Brown R.N., O'Connor J.J. and Armington A.F. (1980) Sweeping and q measurements at elevated temperatures in quartz. *Materials Research Bulletin*, **15**, 1063–1067.
- Brunner G.O., Wondratschek H. and Laves F. (1961) Ultrarotuntersuchungen über den Einbau von H in natürlichem Quarz. *Zeitschrift für Elektrochemie, Berichte der Bunsengesellschaft für physikalische Chemie*, **65**, 735–750.
- Campone P., Magliocco M., Spinolo G. and Vedda A. (1995) Ionic transport in crystalline SiO_2 : The role of alkali-metal ions and hydrogen impurities. *Physical Review B*, **52**, 15903.
- Charlier B.L.A., Morgan D.J., Wilson C.J.N., Wooden J.L., Allan A.S.R. and Baker J.A. (2012) Lithium concentration gradients in feldspar and quartz record the final minutes of magma ascent in an explosive supereruption. *Earth and Planetary Science Letters*, **319–320**, 218–227.
- Cherniak D. (2003) REE diffusion in feldspar. *Chemical Geology*, **193**, 25–41.
- Crank J. (1975) *The Mathematics of Diffusion*. Oxford University Press, Oxford.
- Curie J. (1889) Recherches sur la conductibilité des corps cristallisés. *Annales de chimie et de physique*, **16**, 321–325.
- Darken L.S. and Smith R.P. (1949) Behavior of hydrogen in steel during and after immersion in acid. *Corrosion*, **5**, 1–16.
- Demouchy S. and Mackwell S. (2006) Mechanisms of hydrogen incorporation and diffusion in iron-bearing olivine. *Physics and Chemistry of Minerals*, **33**, 347–355.
- Dohmen R., Kasemann S.A., Coogan L. and Chakraborty S. (2010) Diffusion of Li in olivine. Part i: Experimental observations and a multi species diffusion model. *Geochimica et Cosmochimica Acta*, **74**, 274–292.
- Dolejš D. and Manning C. (2010) Thermodynamic model for mineral solubility in aqueous fluids: Theory, calibration and application to model fluid-flow systems. *Geofluids*, **10**, 20–40.
- Eugster HP and Baumgartner LP (1987) Mineral solubilities and speciation in supercritical metamorphic fluids. Pp. 367–403 in: *Thermodynamic Modeling of Geologic Materials: Minerals, Fluids, and Melts* (I.S.E. Carmichael and H.P. Eugster, editors). Reviews in Mineralogy, Vol. 17, Mineralogical Society of America, Washington DC.
- Frigo C., Stalder R. and Hauenberger C.A. (2016) OH defects in quartz in granitic systems doped with spodumene, tourmaline and/or apatite: Experimental investigations at 5–20 kbar. *Physics and Chemistry of Minerals*, **43**, 717–729.
- Frischat G.H. (1968) Sodium diffusion in SiO_2 glass. *Journal of the American Ceramic Society*, **51**, 528–530.
- Frischat G. (1970) Sodium diffusion in natural quartz crystals. *Journal of the American Ceramic Society*, **53**, 357–357.
- Griggs D.T. and Blacic J.D. (1965) Quartz: Anomalous weakness of synthetic crystals. *Science*, **147**, 292–295.
- Halliburton L., Koumvakalis N., Markes M. and Martin J. (1981) Radiation effects in crystalline SiO_2 : The role of aluminum. *Journal of Applied Physics*, **52**, 3565–3574.
- Hercule S. and Ingrin J. (1999) Hydrogen in diopside: Diffusion, kinetics of extraction-incorporation, and solubility. *American Mineralogist*, **84**, 1577–1587.
- Holycross M. and Watson E.B. (2017) Complex diffusion mechanisms for Li in feldspar: Re-thinking Li-in-plag geospeedometry. *American Geophysical Union, Fall meeting, December 2017, New Orleans, USA*. Abstract V54B-07.
- Hosaka M. and Taki S. (1981) Synthetic quartz crystals grown in NaCl, KCl solutions and pure water, and their low temperature infrared absorption. Pp. 304–311 in: *35th Annual Frequency Control Symposium*. USAERADCOM, Fort Monmouth, New Jersey meeting, May 1981.
- Hughes R.C. (1975) Electronic and ionic charge carriers in irradiated single crystal and fused quartz. *Radiation Effects*, **26**, 225–235.
- Ingrin J. and Blanchard M. (2006) Diffusion of hydrogen in minerals. Pp. 291–320 in: *Water in Nominally Anhydrous Minerals* (H. Keppler and J.R. Smyth, editors). Reviews in Mineralogy and Geochemistry, **62**.

- Mineralogical Society of America and the Geochemical Society, Chantilly, Virginia, USA.
- Jain H. and Nowick A. (1982) Electrical conductivity of synthetic and natural quartz crystals. *Journal of Applied Physics*, **53**, 477–484.
- Jibamitra G., Bhattacharya and S. Chakraborty (1988) Convolution effect in the determination of composition profiles and diffusion coefficients by microprobe step scans. *American Mineralogist*, **73**, 901–909.
- Johnson J.W., Oelkers E.H. and Helgeson H.C. (1992) Supcrt92: A software package for calculating the standard molal thermodynamic properties of minerals, gases, aqueous species, and reactions from 1 to 5000 bar and 0 to 1000°C. *Computers & Geosciences*, **18**, 899–947.
- Jollands M.C. (2020) Assessing analytical convolution effects in diffusion studies: Applications to experimental and natural diffusion profiles. *PLoS one*, **15**.
- Jollands M.C., Ellis B., Tollan P.M.E. and Müntener O. (2020a) An eruption chronometer based on experimentally determined H-Li and H-Na diffusion in quartz applied to the Bishop Tuff. *Earth and Planetary Science Letters*, **551**, 116560.
- Jollands M.C., Blanchard M. and Balan E. (2020b) Structure and theoretical infrared spectra of OH defects in quartz. *European Journal of Mineralogy*, **32**, 311–323.
- Kats A. (1962) Hydrogen in alpha-quartz. *Philips Research Reports*, **17**, 133–195, 201–279.
- King J.C. (1959) The anelasticity of natural and synthetic quartz at low temperatures. *Bell System Technical Journal*, **38**, 573–602.
- Königsberger J. (1897) Über die Absorption von ultrarothem Strahlen in doppeltbrechenden Krystallen. *Annalen der Physik*, **297**, 687–704.
- Kronenberg A.K. (1994) Hydrogen speciation and chemical weakening of quartz. Pp. 123–176 in: *Silica: Physical Behavior, Geochemistry, and Materials Applications* (P.J. Heaney, C.T. Prewitt and G.V. Gibbs, editors). Reviews in Mineralogy and Geochemistry, **29**. Mineralogical Society of America, Washington DC.
- Kronenberg A. and Kirby S.H. (1987) Ionic conductivity of quartz; DC time dependence and transition in charge carriers. *American Mineralogist*, **72**, 739–747.
- Kronenberg A.K., Kirby S.H., Aines R.D. and Rossman G.R. (1986) Solubility and diffusional uptake of hydrogen in quartz at high water pressures: Implications for hydrolytic weakening. *Journal of Geophysical Research: Solid Earth*, **91**, 12723–12741.
- Kurka A., Blanchard M. and Ingrin J. (2005) Kinetics of hydrogen extraction and deuteration in grossular. *Mineralogical Magazine*, **69**, 359–371.
- Mackwell S. and Paterson M. (1985) Water-related diffusion and deformation effects in quartz at pressures of 1500 and 300 MPa. *Point Defects in Minerals*, **31**, 141–150.
- Manning C.E. (1994) The solubility of quartz in H₂O in the lower crust and upper mantle. *Geochimica et Cosmochimica Acta*, **58**, 4831–4839.
- Matthews W., Linnen R.L. and Guo Q. (2003) A filler-rod technique for controlling redox conditions in cold-seal pressure vessels. *American Mineralogist*, **88**, 701–707.
- Merritt E. (1895) Ueber den Dichroismus von Kalkspath, Quarz und Turmalin für ultrarothem Strahlen. *Annalen der Physik*, **291**, 49–64.
- Müller A. and Koch-Müller M. (2018) Hydrogen speciation and trace element contents of igneous, hydrothermal and metamorphic quartz from Norway. *Mineralogical Magazine*, **73**, 569–583.
- Myers M.L., Wallace P.J. and Wilson C.J.N. (2019) Inferring magma ascent timescales and reconstructing conduit processes in explosive rhyolitic eruptions using diffusive losses of hydrogen from melt inclusions. *Journal of Volcanology and Geothermal Research*, **369**, 95–112.
- Ni H. and Zhang Y. (2008) H₂O diffusion models in rhyolitic melt with new high pressure data. *Chemical Geology*, **250**, 68–78.
- Novella D., Jacobsen B., Weber P.K., Tyburczy J.A., Ryerson F.J. and Du Frane W.L. (2017) Hydrogen self-diffusion in single crystal olivine and electrical conductivity of the earth's mantle. *Scientific Reports*, **7**.
- Paterson M.S. (1986) The thermodynamics of water in quartz. *Physics and Chemistry of Minerals*, **13**, 245–255.
- Paton C., Hellstrom J., Paul B., Woodhead J. and Hergt J. (2011) Iolite: Freeware for the visualisation and processing of mass spectrometric data. *Journal of Analytical Atomic Spectrometry*, **26**, 2508–2518.
- Potrafke A., Stalder R., Schmidt B.C. and Ludwig T. (2019) OH defect contents in quartz in a granitic system at 1–5 kbar. *Contributions to Mineralogy and Petrology*, **174**, 98.
- Press W.H., Teukolsky S.A., Vetterling W.T. and Flannery B.P. (2007) *Numerical Recipes 3rd Edition: The Art of Scientific Computing*. Cambridge University Press, Cambridge, UK.
- Roselle GT and Baumgartner L.P. (1995) Experimental determination of anorthite solubility and calcium speciation in supercritical chloride solutions at 2 kbar from 400 to 600°C. *Geochimica et Cosmochimica Acta*, **59**, 1539–1549.
- Rottier B., Rezeau H., Casanova V., Kouzmanov K., Moritz R., Schlöglöva K., Wälle M. and Fontboté L. (2017) Trace element diffusion and incorporation in quartz during heating experiments. *Contributions to Mineralogy and Petrology*, **172**, 23.
- Rovetta M.R., Blacic J.D., Hervig R.L. and Holloway J.R. (1989) An experimental study of hydroxyl in quartz using infrared spectroscopy and ion microprobe techniques. *Journal of Geophysical Research: Solid Earth*, **94**, 5840–5850.
- Rybach L. and Laves F. (1967) Sodium diffusion experiments in quartz crystals. *Geochimica et Cosmochimica Acta*, **31**, 539–545.
- Sartbaeva A., Wells S.A. and Redfern S.A. (2004) Li⁺ ion motion in quartz and β-eucryptite studied by dielectric spectroscopy and atomistic simulations. *Journal of Physics: Condensed Matter*, **16**, 8173.
- Shaffer E.W., Sang J.S.L., Cooper A. and Heuer A. (1974) Diffusion of tritiated water in beta-quartz. Pp 131–138 in: *Proceedings of the Geochemical Transport and Kinetics Conference 1974*. Carnegie Institute of Washington, USA [Publ 634].
- Sibley W., Martin J., Wintersgill M. and Brown J. (1979) The effect of radiation on the OH⁻ infrared absorption of quartz crystals. *Journal of Applied Physics*, **50**, 5449–5452.
- Staats P.A. and Kopp O.C. (1974) Studies on the origin of the 3400 cm⁻¹ region infrared bands of synthetic and natural α-quartz. *Journal of Physics and Chemistry of Solids*, **35**, 1029–1033.
- Stalder R. (2021) OH point defects in quartz – a review. *European Journal of Mineralogy*, **33**, 145–163.
- Stalder R. and Konzett J. (2012) OH defects in quartz in the system quartz–albite–water and granite–water between 5 and 25 kbar. *Physics and Chemistry of Minerals*, **39**, 817–827.
- Tegetmeier F. and Warburg E. (1887) Ueber eine besondere art von electrischer polarisation in krystallen. *Annalen der Physik*, **268**, 442–451.
- Thomas S.-M., Koch-Müller M., Reichart P., Rhede D., Thomas R., Wirth R. and Matsyuk S. (2009) IR calibrations for water determination in olivine, r-GeO₂, and SiO₂ polymorphs. *Physics and Chemistry of Minerals*, **36**, 489–509.
- Tollan P., Ellis B., Troch J. and Neukampf J. (2019) Assessing magmatic volatile equilibria through ftir spectroscopy of unexposed melt inclusions and their host quartz: A new technique and application to the mesa falls tuff, Yellowstone. *Contributions to Mineralogy and Petrology*, **174**, 24.
- Verhoogen J. (1952) Ionic diffusion and electrical conductivity in quartz. *American Mineralogist*, **37**, 637–655.
- Zhang Y. (2010) Diffusion in minerals and melts: Theoretical background. Pp. 5–59 in: *Diffusion in Minerals and Melts* (Y. Zhang and D.J. Cherniak, editors). Reviews in Mineralogy and Geochemistry, **72**. Mineralogical Society of America and the Geochemical Society, Chantilly, Virginia, USA.